PAPER

Check for updates

Synthesis of nano-sized tungsten oxide particles encapsulated in a hollow silica sphere and their photocatalytic properties for decomposition of acetic acid using Pt as a co-catalyst†

Takashi Harada, [iD] *[a] En Yagi[a] and Shigeru Ikeda [iD] [b]

Nano-sized tungsten oxide (WO_3) particles, each of which was encapsulated as a core in a hollow silica sphere ($WO_3@SiO_2$), were synthesized using calcium tungstate particles as the starting material. The calcium tungstate particles, each of which was covered with a silica shell, were converted to tungstic acid by nitric acid treatment and then to WO_3 by heat treatment to obtain $WO_3@SiO_2$. A hollow space was formed in $WO_3@SiO_2$ between the WO_3 core and the SiO_2 shell as a result of shrinkage of WO_3 during the heat treatment. The thus-obtained $WO_3@SiO_2$ was 40 nm in diameter, the WO_3 core was 10 nm in diameter, and the silica shell, which was permeable to gas and liquid, was 10 nm in thickness. $WO_3@SiO_2$ absorbed visible light to the wavelength of 454 nm, which enabled photocatalytic reaction under visible light; Pt was loaded on the WO_3 cores in the photocatalytic reactions. In contrast to Pt-loaded bulk WO_3 photocatalysts without an SiO_2 shell, Pt-loaded $WO_3@SiO_2$ showed continuous and complete decomposition of gaseous acetic acid in air under visible as well as UV irradiation.

Introduction

Titanium dioxide (TiO_2) is well known as the most efficient photocatalyst and has been used in various applications, such as production of renewable energy, decomposition of environmental pollutants and synthesis of useful organic compounds, because electrons and holes photogenerated in TiO_2 have strong reduction and oxidation properties, respectively.[1–3] However, due to its strong oxidation property, TiO_2 indiscriminately decomposes organic compounds, which sometimes leads to problems of decomposition of the support of TiO_2 photocatalyts. To solve this problem, a core–shell structure in which TiO_2 particles are covered with robust inorganic materials has been proposed.[4] The shell is permeable to gas and liquid, while it prevents contact between TiO_2 particles, leading to suppression of degradation of supports made of organic materials. However, the structure had the disadvantage of lowered photocatalytic activity because a large part of the TiO_2 surface, which is important for the photocatalyst, was covered with the shell material. To solve the problem, we have recently developed a TiO_2 photocatalyst encapsulated in a hollow silica shell ($TiO_2@SiO_2$), in which a gap space is formed between the core and the shell. As a result, the $TiO_2@SiO_2$ showed photocatalytic activity as high as that of an intrinsic TiO_2 photocatalyst, and showed size-selectivity for materials to be decomposed, depending on the pore size of the permeable shell.[5–8] In addition, other features of core–hollow shell structure, such as improvement adsorption properties, high temperature stability of core material and application for cascade reaction, have been reported.[9–11]

There have been many efforts to modify TiO_2 so as to enable absorption of visible light; an intrinsic TiO_2 photocatalyst shows low photocatalytic activity in normal environments because it shows photocatalytic activity only under UV light due to its large band gap (3.2 eV). Approaches to solve this problem include doping of TiO_2 with transition metals[12–15] and replacement of oxygen in TiO_2 with sulfur or nitrogen.[16–21] Another approach is to use low band gap materials instead of TiO_2. Tungsten oxide (WO_3) is a good candidate of these materials because of its narrow band gap (2.8 eV), high oxidation property, nontoxicity, and chemical stability.[22] However, a pure WO_3 photocatalyst shows low photocatalytic activity for decomposition of organic compounds because of the low energy level of its conduction band (CB) edge, which is not high enough for the electrons in the CB to reduce O_2 or H_2O. Sayama et al. reported that loading co-catalysts, such as CuO, Pd and Pt, on the surface of WO_3 was effective for improving its photocatalytic activity.[23,24] Although the co-catalysts do not affect the energy level of the CB

[a]*Research Center for Solar Energy Chemistry, Osaka University, 1-3 Machikaneyama, Toyonaka 560-8531, Japan. E-mail: harada@chem.es.osaka-u.ac.jp*

[b]*Department of Chemistry, Faculty of Science and Engineering, Konan University, Okamoto, Higashinada, Kobe 658-8501, Japan*

† Electronic supplementary information (ESI) available: XRD patterns of reference samples. TG-DTA curves time courses for CO_2 evolution and acetic acid decomposition and methanol production during photocatalytic reaction. See DOI: 10.1039/d0ra01988g

of WO_3, they kinetically enhance the electron transfer from WO_3 to O_2 or H_2O and, as a result, increase photocatalytic activity of WO_3. We expect that WO_3 particles encapsulated in a hollow silica sphere (WO_3@SiO_2) would be suitable as a photocatalyst used under visible light.

A number of synthesis procedures have been developed to produce the core–hollow shell structure using, for example, the Kirkendall effect,[25] a hard template,[26] and an etching process.[27] We previously reported the synthesis of TiO_2@SiO_2 using a carbon material as a hard template.[5–8] The hard template method is useful for obtaining well-defined core–hollow shell structures.[5–8,26] However, this method requires the formation and removal of solid templates, which are troublesome procedures, especially for practical use. Moreover, core–hollow shell structures thus-obtained are often large in size and irregular in shape. Because these structures show low mechanical stability due to the large hollow space, the structure needs to be small and, ideally, spherical.

We recently developed a simple procedure for making nickel nanoparticles encapsulated in a hollow silica sphere.[28] In this procedure, small crystals of a nickel hydrazine complex were prepared in a reverse microemulsion system and were directly covered with a silica layer. The nickel hydrazine crystals were converted to nickel nanoparticles by heat treatment. Because the nickel nanoparticles were smaller than nickel hydrazine crystals, a core–hollow shell structure was automatically obtained during the heat treatment. Here, we applied this strategy to the synthesis of WO_3@SiO_2 and evaluated its photocatalytic activity for decomposition of acetic acid in gas phase, which was used as a model reaction.

Experimental

Synthesis of tungsten oxide photocatalysts

Tungsten oxide encapsulated in a hollow silica sphere (WO_3@SiO_2) was synthesized as follows. To 34 g polyoxyethylene cetyl ether ($n = 15$) (30 mmol) dissolved in 75 cm^3 of cyclohexane were added 4.5 cm^3 of 0.1 M aqueous $Ca(NO_3)_2$ (0.45 mmol) and 4.5 cm^3 of 0.1 M aqueous Na_2WO_4 (0.45 mmol). After the mixture had been stirred at 55 °C for 1 h, 1.5 cm^3 of hydrazine monohydrate (30 mmol) was added and the mixture was stirred at 55 °C for 1 h. Then 3 cm^3 of tetraethylorthosilicate (TEOS: 13.4 mmol) was added to the suspension, which was stirred at 55 °C for 2 h. After addition of 240 cm^3 of 2-propanol to the suspension, the mixture was centrifuged (3000 rpm, 4 min) to recover the precipitate, which was washed with 2-propanol three times. The precipitate was added to 2.5 M aqueous HNO_3 at 80 °C for 6 h and then washed with distilled water until the effluent showed neutral pH. After drying at 80 °C, the powder was calcined at 700 °C for 2 h in air to produce WO_3@SiO_2.

As a reference photocatalyst, we synthesized bulk WO_3 (WO_3(B)) powder by the same procedure but without the use of the reverse micelle system and silica source. WO_3(B) physically mixed with SiO_2 (WO_3(B)/SiO_2) was also used as a reference photocatalyst. This reference photocatalyst was prepared using H_2WO_4, which is a precursor of WO_3(B), and about 30 nm of

SiO_2 powder, which is synthesized by a slightly modified Stöber method.[29] They were mechanically mixed and calcined at 700 °C. The WO_3 content of WO_3(B)/SiO_2 was adjusted to be the same as that of WO_3@SiO_2.

Characterization

TEM images were taken on a Hitachi H-9000NAR instrument operated at 300 kV. Powder X-ray diffraction (XRD) patterns were recorded using a Rigaku MiniFlex X-ray diffractometer (CuKα, Ni filter). Analyses of the surface area and pore structure were carried out using a Quantachrome AUTOSORB-1 automated gas-sorption system with N_2 as the adsorbate, after pretreatment of the sample at 200 °C for 2 h under reduced pressure. The BET surface area was calculated from the adsorption branch of the isotherm. Ultraviolet and visible-light diffuse reflection (UV-vis DR) spectra were obtained with a Hitachi U-4100 UV-vis-NIR spectrometer equipped with an integrating sphere using $BaSO_4$ as a reference. The reflectance spectra were converted to absorbance spectra by the Kubelka–Munk method.

Photocatalytic decomposition of acetic acid in gaseous phase

Photocatalytic decomposition of acetic acid was carried out over Pt-loaded WO_3 photocatalysts (Pt/WO_3) in gaseous phase. Pt-loading on WO_3 photocatalysts was carried out by the photodeposition method sequentially from an aqueous methanol (10 vol%) solution of $H_2PtCl_6 \cdot 6H_2O$.[30] The loading amount of Pt was fixed at 0.5 wt% of WO_3 for all of the photocatalysts.

Photocatalytic decomposition of acetic acid was performed in a 225 cm^3 Pyrex cylindrical reaction vessel (64 mm in diameter) with a quartz top window. The photocatalyst, containing 30 mg of WO_3, was spread on the slide glass (38 mm × 26 mm) and set in the vessel. After closing the vessel, 1 μl of acetic acid (17.5 μmol) was introduced into the vessel. After acetic acid had been fully vaporized and had reached an absorption equilibrium in the vessel, the sample was photoirradiated with a 300 W Xe lamp though the quartz top window. CO_2 was analyzed with a Shimadzu GC-8A gas chromatograph equipped with a TCD detector and an activated carbon column, and organic compounds were analyzed with a Shimadzu GC-2014 gas chromatograph equipped with a BID detector and a TC-FFAP column. For the analyses, a portion of the gas phase was sampled with an air-tight syringe at appropriate intervals.

Results and discussion

Synthesis and characterizations of tungsten oxide nanoparticles encapsulated in a hollow silica sphere

Synthesis of nano-sized WO_3@SiO_2 was performed in a water in oil (W/O) microemulsion system. In the first step, an aqueous $Ca(NO_3)_2$ solution was added to a cyclohexane solution containing polyoxyethylene cetyl ether ($n = 15$) to form a W/O microemulsion. Addition of an aqueous Na_2WO_4 solution into the W/O microemulsion solution induced a color change from transparent to white; it became turbid after a while, indicating formation of solid components. By adding a hydrazine

monohydrate solution and TEOS to this solution, poly-condensation of the siliceous component was continuously carried out. After 2 h agitation of the mixture, the solid part was collected. Fig. 1a shows an XRD pattern of the thus-obtained white powder. All of the peaks were assigned to $CaWO_4$ as referred from the JCPDS card (no. 41-1431). A TEM image of the white powder showed spherical core–shell structure (Fig. 2a). These results indicate that $CaWO_4$ particles were directly covered with a silica shell ($CaWO_4@SiO_2$). The diameter of the $CaWO_4$ core was 10–20 nm and the thickness of the silica shell was about 10 nm.

The thus-obtained $CaWO_4@SiO_2$ powder was treated with aqueous HNO_3 solution at 80 °C for 6 h. During HNO_3 treatment, the white color of the turbid solution gradually changed to yellow. The corresponding XRD pattern of the thus-obtained yellow powder was assigned to H_2WO_4 as referred from the JCPDS card (no. 43-0679) (Fig. 1b). The TEM image showed that the core–shell structure was not changed by the HNO_3 treatment, as shown in Fig. 2b. These results indicate that the $CaWO_4$ core particle of $CaWO_4@SiO_2$ was converted to H_2WO_4 by the HNO_3 treatment and that a core–shell material having an H_2WO_4 core and a silica shell ($H_2WO_4@SiO_2$) was obtained.

After calcination of $H_2WO_4@SiO_2$ at 700 °C, the color changed to light green. The XRD pattern of this sample showed the formation of monoclinic WO_3 (JCPDS card no. 43-1035) (Fig. 1c), which was obtained by dehydration of H_2WO_4. To confirm dehydration of H_2WO_4, thermogravimetric-differential thermal analysis (TG-DTA) was carried out. The TG-DTA curves of $H_2WO_4@SiO_2$ were shown in Fig. S2.† A weight loss with endothermic peak was observed at around 100 °C and 200 °C. These are due to desorption of physically adsorbed water molecule on $H_2WO_4@SiO_2$ particles and coordinated water molecules of H_2WO_4, respectively. A weight loss of exothermic peak was observed at 250–700 °C, due to combustion of surfactant and siliceous compounds including removal of residual coordinated water.[31] A TEM image and high resolution TEM (HRTEM) image of this sample are shown in Fig. 2c and inset of Fig. 2c, respectively. In contrast to the TEM image of
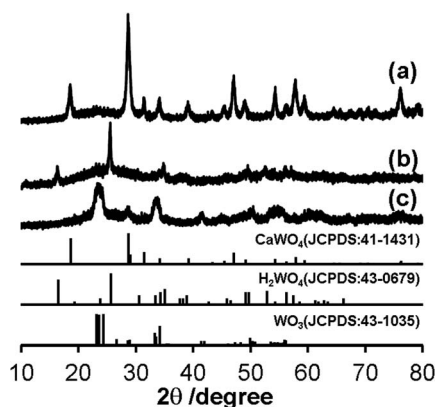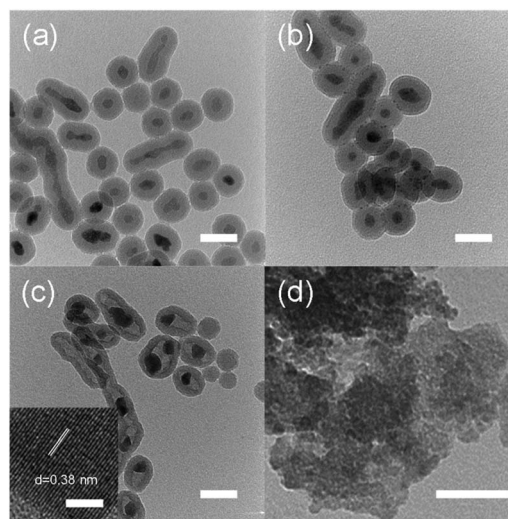

Fig. 2 TEM images of (a) $CaWO_4@SiO_2$, (b) $H_2WO_4@SiO_2$, (c) $WO_3@SiO_2$ and (d) $WO_3(B)$. Scale bars are corresponding to 40 nm. Inset of (c) is HRTEM image of $WO_3@SiO_2$ and scale bar is corresponding to 5 nm.

$H_2WO_4@SiO_2$, a hollow space was observed in this sample, indicating the formation of WO_3 encapsulated in a hollow silica sphere ($WO_3@SiO_2$). The hollow space was caused by shrinkage of the volume as H_2WO_4 was converted to WO_3. The size of the WO_3 particles was about 10 nm in diameter, which is smaller than that of the H_2WO_4 core in $H_2WO_4@SiO_2$. The lattice fringes of HRTEM image of WO_3 particle are assigned to the (100) plane of monoclinic WO_3. This is agreement with the XRD result. The silica shell thickness seems to be slightly decreased after the heat treatment. A TEM image of $WO_3(B)$ powder that was prepared without using the reverse microemulsion system and silica source showed that the particle size was large and inhomogeneous (40–100 nm) as can be seen in Fig. 2d, although $WO_3(B)$ was obtained by the same route as $WO_3@SiO_2$ (Fig. S1†). These results suggest that the use of the reverse microemulsion system and the silica shell structure are effective for suppressing the growth of WO_3 particles during calcination.

Fig. 3 shows N_2 adsorption–desorption isotherms of $WO_3(B)$, $CaWO_4@SiO_2$ and $WO_3@SiO_2$ samples. The isotherm of $WO_3(B)$ is classified as characteristic type III according to the IUPAC nomenclature and the BET surface area is 13 m^2 g^{-1}, indicating a nonporous structure. The isotherm of $CaWO_4@SiO_2$ is classified as characteristic type II and showed a slight increase in N_2 uptake at a relative pressure (P/P_0) below 0.1, indicating the existence of micropores in the silica shell. The BET surface area of $CaWO_4@SiO_2$ was found to be 65 m^2 g^{-1}. The isotherm of $WO_3@SiO_2$ showed a characteristic type IV with a hysteresis loop and the BET surface area was 175 m^2 g^{-1}. Compared with $CaWO_4@SiO_2$, $WO_3@SiO_2$ showed a steep increase in N_2 uptake at P/P_0 below 0.1, indicating the formation of a well-developed micropore system probably due to removal of the surfactant in the silica shell during high temperature calcination. Moreover, a hysteresis loop enclosed at a P/P_0 of *ca.* 0.4–0.9 was observed. These phenomena are attributed to the tensile

Fig. 1 XRD patterns of (a) $CaWO_4@SiO_2$, (b) $H_2WO_4@SiO_2$ and (c) $WO_3@SiO_2$. The standard data of $CaWO_4$ (JCPDS: 41-1431), H_2WO_4 (JCPDS: 43-0679) and WO_3 (JCPDS: 43-1035) are shown as a reference.
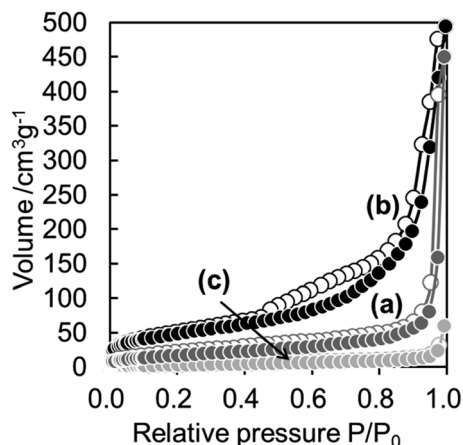
Fig. 3 N_2 sorption isotherms of (a) $CaWO_4@SiO_2$, (b) $WO_3@SiO_2$ and (c) $WO_3(B)$. Filled and open circles denote adsorption and desorption isotherms, respectively.

strength effect observed in materials having a hollow structure encapsulated by a pore system of relatively small pore size.[32] These results are in agreement with the TEM images and indicate the formation of a hollow structure with a well-developed pore system in the silica shell.

The content of the WO_3 component in $WO_3@SiO_2$ was estimated by the gravimetric method. The weight of the WO_3 component in $WO_3@SiO_2$ was measured after etching the SiO_2 component by diluted HF aqueous solution; we confirmed in advance that WO_3 was not dissolved in the dilute HF aqueous solution. From the measurement, the WO_3 content was found to be 60 wt% of $WO_3@SiO_2$.

UV/Vis diffuse reflectance spectra of $WO_3@SiO_2$ and $WO_3(B)$ powders are shown in Fig. 4. Reflectance is converted to absorbance by the Kubelka–Munk equation:

$$F(R) = (1 - R)^2/2R, \qquad (1)$$

where $F(R)$ denotes Kubelka–Munk function and R denotes reflectance of the sample relative to that of a non-absorbing
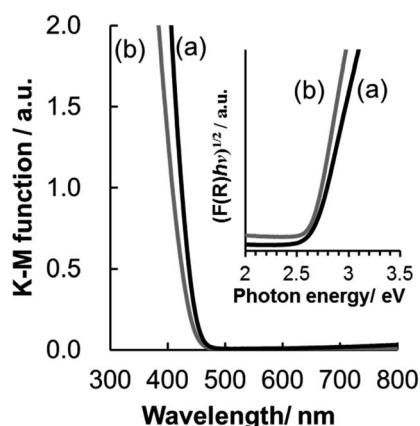
standard ($BaSO_4$). The spectra indicate that the on-set values of the absorption bands are located at 454 and 486 nm for $WO_3@SiO_2$ and $WO_3(B)$, respectively. Considering that WO_3 is an indirect n-type semiconductor, its energy band gap (E_g) can be determined by optical absorption measurements using the following relationship:[33]

$$(F(R)h\nu)^{1/2} = K(h\nu - E_g), \qquad (2)$$

where $h\nu$ the incident photon energy and K is a constant. The inset in Fig. 4 shows plots of $(F(R)h\nu)^{1/2}$ versus $h\nu$. By extrapolating the plots linearly, the energy band gaps of $WO_3@SiO_2$ and $WO_3(B)$ are estimated to be 2.65 and 2.63 eV, respectively. The estimated energy band gaps are in good agreement with the values (2.5–2.8 eV) reported in the literature.[34] The reflectance spectrum of the $WO_3@SiO_2$ powder showed a slight blue shift compared with that of the bulk $WO_3(B)$ powder, probably due to the differences of WO_3 particle size and/or crystallinity.[35,36]

Photocatalytic decomposition of acetic acid

Photocatalytic decomposition of acetic acid in gaseous phase was used as a measure of photocatalytic activity of WO_3 having different morphologies. Since WO_3 photocatalysts show poor catalytic activity for decomposition of organic compounds due to their low reduction property, we loaded a Pt co-catalyst on WO_3 particles of all of the photocatalysts we examined; these particles are denoted by Pt/WO_3.

A comparison of time courses of CO_2 evolution during decomposition of acetic acid under full-arc irradiation from a 300 W Xe lamp with various Pt-loaded WO_3 photocatalysts and TiO_2 photocatalyst made of commercially available TiO_2 (ST-01, Ishihara Sangyo Co. Ltd.) is shown in Fig. 5. In 100 min, the TiO_2 and $Pt/WO_3@SiO_2$ photocatalysts produced CO_2 continuously to the level of 35 μmol, which corresponds to the stoichiometric amount of the introduced acetic acid (17.5 μmol), indicating complete decomposition of acetic acid. The initial high rate of CO_2 evolution with the TiO_2 photocatalyst seems to be due to its intrinsically high photocatalytic activity. However,
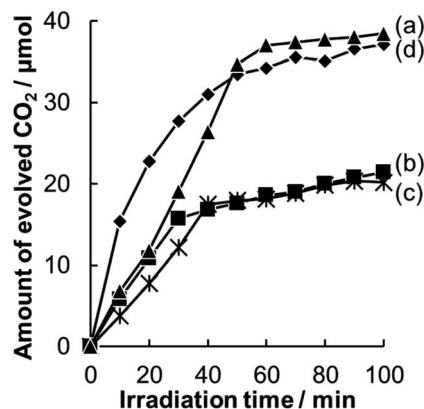

Fig. 4 UV-visible diffuse reflectance spectrum of (a) $WO_3@SiO_2$ and (b) $WO_3(B)$.

Fig. 5 Time courses for CO_2 evolution during photocatalytic decomposition of acetic acid over (a) $Pt/WO_3@SiO_2$, (b) $Pt/WO_3(B)$, (c) $Pt/WO_3(B)/SiO_2$ and (d) TiO_2 (ST-01) under full-arc light irradiation from a 300 W Xe lamp.

the WO$_3$ photocatalyts (Pt/WO$_3$@SiO$_2$ and Pt/WO$_3$(B)) showed much higher activity than that of the TiO$_2$ photocatalyst, as shown in Fig. 6, suggesting the usefulness of WO$_3$ photo-catalysts under visible light conditions. Of the WO$_3$ photo-catalyts, Pt/WO$_3$@SiO$_2$ was effective for complete decomposition of acetic acid, as shown in Fig. 5 and 6.

In Fig. 5, Pt/WO$_3$@SiO$_2$ and Pt/WO$_3$(B)/SiO$_2$ show concave slopes for CO$_2$ evolution in the initial period. This unique property of the photocatalysts seems to be related to the hollow shell structure. We consider that the release of CO$_2$ from the hollow space of the photocatalysts to the outer space is hindered to some extent by the porous SiO$_2$ shell, leading to the concave slope until the concentration of CO$_2$ reaches a certain level. For the same reason, we can expect that reactive products produced in the hollow space have as higher chance of reaction on the photocatalyst because their escape from the hollow space and supply of acetic acid to the hollow space are hindered by the silica shell. The concentration of the intermediate in the hollow shell of Pt/WO$_3$@SiO$_2$ can be lower than that of Pt/WO$_3$(B) in the gas phase because the intermediate competes with acetic acid for the reaction sites (or photogenerated holes) on WO$_3$. Such a function of the hollow shell (or hollow shell effect) will affect the activity of the photocatalysts as mentioned later.

Pt/WO$_3$@SiO$_2$ and Pt/WO$_3$(B) showed almost the same reaction rates for CO$_2$ evolution during the initial reaction period, as shown in Fig. 5. However, the evolution rate of CO$_2$ with Pt/WO$_3$(B) decreased drastically when the amount of CO$_2$ reached half of the stoichiometric level, suggesting that meth-anol or formaldehyde, both of which are the chief intermediates for decomposition of acetic acid, accumulates in the system. To confirm this assumption, we added acetic acid to the system with Pt/WO$_3$(B) after the CO$_2$ evolution rate had decreased and we found that the CO$_2$ evolution rate almost recovered to the initial rate (Fig. S3†). This result strongly suggests that the decrease in the CO$_2$ evolution rate with Pt/WO$_3$(B) is not due to poisoning of the active sites of WO$_3$ but is due to the slow decomposition rate of the intermediate. This is also consistent

with the fact that CO$_2$ evolution continued even after the CO$_2$ evolution rate had decreased over Pt/WO$_3$(B).

To confirm the effect of the intermediates, products in the gas phase were analyzed during the photocatalytic reaction. As a result, methanol was observed in the gas phase together with very small amounts of methyl formate and methyl acetate. However, formaldehyde was not observed. It is well known that formaldehyde is the major oxidation product from methanol.[37] Formaldehyde was not detected in this system probably because formaldehyde was strongly adsorbed on the photocatalysts or decomposed rapidly. The amount of methanol over Pt/WO$_3$@SiO$_2$ was smaller than that over Pt/WO$_3$(B) (Fig. S4†). This result is consistent with the hollow shell effect mentioned above.

In the case of Pt/WO$_3$(B), even after methanol and other intermediates had been completely decomposed, the amount of CO$_2$ was insufficient for a stoichiometric amount, indicating that the formaldehyde produced is strongly adsorbed on Pt/WO$_3$(B). Formaldehyde is easily polymerized to a stable para-formaldehyde at a high concentration as reported in the liter-ature.[38,39] Since paraformaldehydes are relatively difficult to decompose, the CO$_2$ evolution rate is drastically reduced if they accumulate on the photocatalyst.

In the case of the hollow space of Pt/WO$_3$@SiO$_2$, however, the sequential photo decomposition reaction of intermediates proceeds efficiently due to the hollow shell effect, which maintains the concentration of formaldehyde at a low level. As a result, formation of paraformaldehyde was probably sup-pressed and continuous complete decomposition of acetic acid was achieved. The catalytic activity of Pt/WO$_3$(B)/SiO$_2$, which is physically mixed WO$_3$(B) with SiO$_2$, was almost the same as that of Pt/WO$_3$(B). These results indicate that the hollow structure, not the SiO$_2$ content, is important for the complete decompo-sition of acetic acid. Although further studies are needed to understand the detailed reaction mechanisms, the hollow structure is expected to be effective for the photodecomposition of organic compounds through stable intermediates.

Conclusions

We developed a procedure for the synthesis of WO$_3$ nano-particles encapsulated in a hollow silica sphere by effectively using a reverse micelle system and volume change of tungsten compounds. The obtained core–hollow shell structure was composed of WO$_3$ nanoparticles of 10 nm in diameter and a porous SiO$_2$ shell of 10 nm in thickness with highly developed micropores. The core–hollow shell structure of Pt-loaded WO$_3$@SiO$_2$ has great advantages in photocatalytic applica-tions, as exemplified by the continuous and complete decom-position of acetic acid, compared to other bulk WO$_3$ photocatalyts. The findings will lead to further improvement in the catalytic activity of WO$_3$@SiO$_2$ by an optimized core–hollow shell structure.

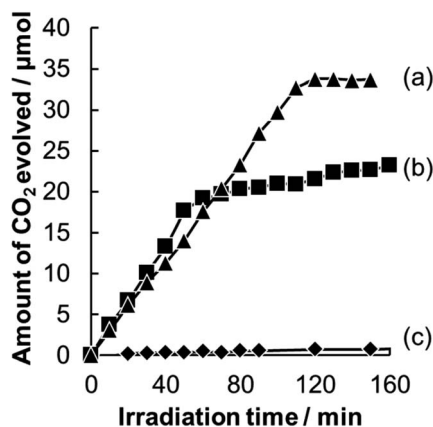**Fig. 6** Time courses for CO$_2$ evolution during photocatalytic decomposition of acetic acid over (a) Pt/WO$_3$@SiO$_2$, (b) Pt/WO$_3$(B) and (c) TiO$_2$ (ST-01) under visible light irradiation (λ > 400 nm).

Conflicts of interest

There are no conflicts to declare.

Acknowledgements

References

1 M. R. Hoffmann, S. T. Martin, W. Choi and D. W. Bahnemann, *Chem. Rev.*, 1995, **95**, 69.

2 A. Fujishima, K. Hashimoto and T. Watanabe, *TiO₂ Photocatalysis Fundamentals and Applications*, BKC, Tokyo, 1999, p. 176.

3 A. Fujishima, T. N. Rao and D. A. Tryk, *J. Photochem. Photobiol., C*, 2000, **1**, 1.

4 H. S. Lee, S. M. Koo and J. W. Yoo, *J. Ceram. Process. Res.*, 2012, **13**, s300.

5 S. Ikeda, Y. Ikoma, H. Kobayashi, T. Harada, B. Ohtani, T. Torimoto and M. Matsumura, *Chem. Commun.*, 2007, 3753.

6 S. Ikeda, H. Kobayashi, Y. Ikoma, T. Harada, T. Torimoto, B. Ohtani and M. Matsumura, *Phys. Chem. Chem. Phys.*, 2007, **9**, 6319.

7 S. Ikeda, H. Kobayashi, T. Sugita, Y. Ikoma, T. Harada and M. Matsumura, *Appl. Catal., A*, 2009, **363**, 216.

8 S. Ikeda, H. Kobayashi, Y. Ikoma, T. Harada, S. Yamazaki and M. Matsumura, *Appl. Catal., A*, 2009, **369**, 113.

9 W. Zhang, X.-J. Lin, Y.-G. Sun, D.-S. Bin, A.-M. Cao and L.-J. Wan, *ACS Appl. Mater. Interfaces*, 2015, **7**, 27031–27034.

10 Y. Kuwahara, Y. Sumida, K. Fujiwara and H. Yamashita, *ChemCatChem*, 2016, **8**, 2781–2788.

11 Y. Yang, X. Liu, X. Li, J. Zhao, S. Bai, J. Liu and Q. Yang, *Angew. Chem., Int. Ed.*, 2012, **51**, 9164–9168.

12 T. Umebayashi, T. Yamaki, H. Itoh and K. Asai, *J. Phys. Chem. Solids*, 2002, **63**, 1909–1920.

13 N. Murakami, T. Chiyoya, T. Tsubota and T. Ohno, *Appl. Catal., A*, 2008, **348**, 148.

14 C. Wang, Z. Chen, H. Jin, C. Cao, J. Lia and Z. Mib, *J. Mater. Chem. A*, 2014, **2**, 17820.

15 V. Moradi, M. B. G. Jun, A. Blackburn and R. A. Herring, *Appl. Surf. Sci.*, 2018, **427**, 791.

16 R. Asahi, T. Morikawa, T. Ohwaki, K. Aoki and Y. Taga, *Science*, 2001, **293**, 269.

17 G. R. Torres, T. Lindgren, J. Lu, C.-G. Granqvist and S.-E. Lindquist, *J. Phys. Chem. B*, 2004, **108**, 5995.

18 H. Irie, Y. Watanabe and K. Hashimoto, *J. Phys. Chem. B*, 2003, **107**, 5483.

19 H. Irie, Y. Watanabe and K. Hashimoto, *Chem. Lett.*, 2003, **32**, 772.

20 T. Ohno, T. Tsubota, K. Nakajima and Z. Miyamoto, *Chem. Lett.*, 2004, **33**, 750.

21 T. Umebayashi, T. yamaki, S. Tanaka and K. Asai, *Chem. Lett.*, 2003, **32**, 330.

22 G. Xin, W. Guo and T. Ma, *Appl. Surf. Sci.*, 2009, **256**, 165.

23 T. Arai, M. Yanagida, Y. Konishi, Y. Iwasaki, H. Sugihara and K. Sayama, *Catal. Commun.*, 2008, **9**, 1254.

24 T. Arai, M. Horiguchi, M. Yanagida, T. Gunji, H. Sugihara and K. Sayama, *Chem. Commun.*, 2008, 5565.

25 Y. Yin, R. M. Rioux, C. K. Erdonmez, S. Hughes, G. A. Somorjai and A. P. Alivisatos, *Science*, 2004, **304**, 711.

26 T. Harada, S. Ikeda, Y. H. Ng, T. Sakata, H. Mori, T. Torimoto and M. Matsumura, *Adv. Funct. Mater.*, 2008, **18**, 2190.

27 J. Lee, J. C. Park and H. Song, *Adv. Mater.*, 2008, **20**, 1523; J. C. Park, J. U. Bang, J. Lee, C. H. Ko and H. Song, *J. Mater. Chem.*, 2010, **20**, 1239.

28 T. Harada, T. Misaka, T. Sakata, S. Ikeda and M. Matsumura, *Appl. Mech. Mater.*, 2013, **372**, 132.

29 W. Stöber, A. Fink and E. J. Bohn, *J. Colloid Interface Sci.*, 1968, **26**, 62.

30 R. Abe, H. Takami, N. Murakami and B. Ohtani, *J. Am. Chem. Soc.*, 2008, **130**, 7780.

31 J. Cao, B. Luo, H. Lin, B. Xu and S. Chen, *Appl. Catal., B*, 2012, **111–112**, 288.

32 J. C. Groen, L. A. A. Peffer and J. P. Trez-RamRez, *Microporous Mesoporous Mater.*, 2003, **60**, 1.

33 A. Chithambararaj and A. C. Bose, *Beilstein J. Nanotechnol.*, 2011, **2**, 585.

34 M. A. Butler, *J. Appl. Phys.*, 1997, **48**, 1914.

35 H. Kominami, K. Yabutani, T. Yamamoto, Y. Keraa and B. Ohtani, *J. Mater. Chem.*, 2001, **11**, 3222.

36 G. W. Ho, K. J. Chua and D. R. Siow, *Chem. Eng. J.*, 2012, **181–182**, 661.

37 M. Kawai, T. Kawai, S. Naito and K. Tamaru, *Chem. Phys. Lett.*, 1984, **110**, 58.

38 J. L. Davis and M. A. Barteau, *J. Am. Chem. Soc.*, 1989, **111**, 1782.

39 A. K. Chakraborty, S. Y. Chai and W. I. Lee, *Bull. Korean Chem. Soc.*, 2008, **2**, 494.